

Geophysical Research Letters



RESEARCH LETTER

10.1029/2021GL093874

Special Section:

The Exceptional Arctic Polar Vortex in 2019/2020: Causes and Consequences

Key Points:

- Trajectories of fluid parcels during vortex rupture are shown
- Lagrangian coherent structures with a special configuration of flow barriers are identified in the vortex split
- Trajectory analysis shows how ozone poorest air remains in the main vortex over Eurasia at the split while ozone-poor air moves over Canada

Supporting Information:

Supporting Information may be found in the online version of this article.

Correspondence to:

J. Curbelo,
jezabel.curbelo@upc.edu

Citation:

Curbelo, J., Chen, G., & Mechoso, C. R. (2021). Lagrangian analysis of the northern stratospheric polar vortex split in April 2020. *Geophysical Research Letters*, 48, e2021GL093874. <https://doi.org/10.1029/2021GL093874>

Received 15 APR 2021

Accepted 21 JUL 2021

© 2021. The Authors.

This is an open access article under the terms of the [Creative Commons Attribution-NonCommercial-NoDerivs License](https://creativecommons.org/licenses/by-nc-nd/4.0/), which permits use and distribution in any medium, provided the original work is properly cited, the use is non-commercial and no modifications or adaptations are made.

Lagrangian Analysis of the Northern Stratospheric Polar Vortex Split in April 2020

Jezabel Curbelo¹ , Gang Chen² , and Carlos Roberto Mechoso² 

¹Departament de Matemàtiques, Universitat Politècnica de Catalunya, Barcelona, Spain, ²Department of Atmospheric and Oceanic Sciences, University of California, Los Angeles, CA, USA

Abstract The present study examines the northern stratosphere during April 2020, when the polar vortex split into two cyclonic vortices during a winter-early spring period with the strongest ozone depletion on record. We investigate the dynamical evolution leading to the split at middle stratospheric levels, including the fate of fluid parcels on the vortex boundary during its rupture and the distribution of ozone between the vortices resulting from the split. We also illustrate the vertical structure of the vortices after the split. The findings obtained with Lagrangian methods confirm the key role for the split played by a flow with a special configuration of barriers to the motion of parcels. A trajectory analysis clarifies how the ozone distribution between vortices was such that ozone poorest air remained in the main vortex. The offspring vortex had a deep structure from the troposphere and later decayed to vanish by the end of April.

Plain Language Summary The Northern Hemisphere stratosphere during boreal winter and early spring 2020 had multiple outstanding features. The period showed the strongest ozone depletion on record for the hemisphere accompanied by very low temperatures. The stratospheric evolution included an episode of polar warming at upper levels in March. These features have motivated several studies. In mid-April 2020, the polar vortex split into two cyclonic vortices at the middle and lower levels of the stratosphere. A mass of ozone-poor air that had persisted within the westerly circulation throughout the period also split with the polar vortex. We search for the answer to several outstanding questions in stratospheric dynamics and tracer evolution: What flow structures lead to the vortex split? How were air parcels with different ozone concentrations distributed between the vortices during the split? Our approach is based on following parcels trajectories and examining barriers to tracer transport. We highlight the special polar configuration associated with stratospheric vortex splits. A trajectory analysis gives insight into the transport of ozone between the vortices during the split. We also illustrate the vertical structure of the vortices after the split.

1. Introduction

The Northern Hemisphere stratosphere during boreal winter and early spring of 2020 was remarkable in several ways. The polar night vortex was strong and persistent from December to February, while wave activity input from the troposphere was low and the Arctic Oscillation was in an unprecedentedly strong positive phase (Hardiman et al., 2020; Lawrence et al., 2020; Lee et al., 2020). The lowest values of stratospheric ozone on record were observed during the period (Dameris et al., 2021; Inness et al., 2020; Manney et al., 2020; Wohltmann et al., 2020) and the Arctic ultraviolet radiation was unusually high at the surface (Bernhard et al., 2020). Around mid-March, a warming amounting to tens of Kelvin developed in the upper stratosphere of the polar region. Temperatures inside the vortex remained below the threshold for Type I polar stratospheric clouds from early December to late March (the longest period on record) (see Bognar et al., 2021). Around mid-April 2020, when column ozone in the north polar region was achieving record low values (Dameris et al., 2021), the cyclonic vortex became distorted and split on April 22 into two cyclonic vortices from the upper troposphere to the middle stratosphere. One of the resulting vortices was established over Eurasia while a second one developed over North America. These two vortices remained distinct for a few days. The lowest ozone mixing ratio values (O_3) remained within the vortex over Eurasia while ozone-poor air set over Canada. Afterward, the second vortex over North America decayed and the westerly circulation weakened following the seasonal evolution to summer conditions.

Several studies have examined the relatively rare vortex splits in the stratosphere to gain insight on whether the air parcels in the secondary vortex, formed after split, come from preferred locations (such as the periphery) of the main vortex. The event that occurred in the northern stratosphere in February and early March 1979 during the period of the First Global Atmospheric Research Program (GARP) Global Experiment (FGGE) attracted considerable attention (Jung et al., 2001, and references therein). One of these studies (Manney et al., 1994) simulated the entire evolution of the event with numerical, primitive-equation models of the stratosphere-mesosphere. These authors described the evolution of a split as consisting of a period of enhanced upward propagation of wave activity and breakdown of the main polar vortex consolidated by the intrusion of a narrow tongue of air from the tropics into the polar region between the resulting vortices, after which these recombined to form a single vortex. Manney et al. (2015) and Manney and Lawrence (2016) used several diagnostic tools to examine polar vortex splits in 2012/2013 and 2015/2016, respectively, from the perspective of polar chemical processing and ozone depletion. One of the tools was the Lagrangian descriptor known as the function M (Mancho et al., 2013), which they used to show a synoptic picture of the strength of the vortex transport barrier revealing local variations consistent with the evolution of long-lived tracer gases. Manney et al. (2015) showed that the major sudden warming of the split-type in 2012/2013 briefly enhanced ozone loss. The Arctic polar vortex in the 2015/2016 winter was persistently strong and cold and it was cut short because of a vortex split that occurred at the beginning of March, which prevented a significant stratospheric ozone deficit (Manney & Lawrence, 2016). The methodology of these studies was based on examining the time evolutions of several variables expressed as a function of equivalent latitude complemented by synoptic maps.

The present study examines the stratospheric vortex split on April 2020 and associated features in the ozone distribution. Unlike the studies mentioned in the previous paragraph, our approach is entirely based on Lagrangian tools (more specifically on the function M). We discuss the advantages of this methodology in our study of the unique vortex split event in the southern stratosphere during September 2002 (Curbelo et al., 2019a, 2019b). The main power of the Lagrangian analysis is the information it provides on coherent structures of the flow (e.g., the hyperbolic trajectories [HTs]) as well as the boundaries separating regions in which parcels have a different dynamical fate. An M -based strategy, therefore, allows us to narrow down on the behavior of parcels that form the boundaries of the vortices and to examine in detail the behaviors of barriers to the flow, that is, invariant manifolds, which are represented by the singular features of M as explained in the next section. In addition, HTs have been associated with Kelvin's "cat's eye" patterns (Stewartson, 1977; Warn & Warn, 1978) generated by planetary waves breaking at the critical levels (Guha et al., 2016). The outcome of the analysis presented here is a detailed view of how the boundary of the main vortex ruptured to enclose two vortices. Furthermore, we narrow down on the parcels in the main vortex transferred to the secondary vortex and the resulting ozone distribution between vortices. We refer to the vortex over Eurasia as the main vortex or Eurasia vortex and to that over North America as the secondary, offspring or North America vortex. For this, we focus on the trajectories of sets of parcels encapsulated by manifolds.

We start in Section 2 with a description of data and the Lagrangian tool used. Section 3 is a description of the flow with an emphasis on the period from April 10 to the vortex split on April 22. Section 4 examines the distribution of fluid parcels between the vortices resulting from the split. Our conclusions are presented in Section 5.

2. Data and Methods

We use data from ERA5, the fifth generation ECMWF atmospheric reanalysis of the global climate Copernicus Climate Change Service (C3C) (Hersbach et al., 2018). The data provides wind velocity (m s^{-1}), geopotential ($\text{m}^2 \text{s}^{-2}$), potential vorticity ($\text{K m}^2 \text{kg}^{-1} \text{s}^{-1}$) and O_3 (kg kg^{-1}). The spatial resolution of the data we analyze is $0.25^\circ \text{lon.} \times 0.25^\circ \text{lat.}$ with 37 pressure levels. The temporal resolution of the data is 1 h, which is the highest available in the data set.

Our Lagrangian descriptor of choice is the function M (Mancho et al., 2013). This is defined by the expression,

$$M(\mathbf{x}_0, t_0, \tau) = \int_{t_0 - \tau}^{t_0 + \tau} \|\mathbf{v}(\mathbf{x}(t; \mathbf{x}_0), t)\| dt, \quad (1)$$

where $\mathbf{v}(\mathbf{x}, t)$ is the two-dimensional (2D) velocity field on isentropic surfaces and $\|\cdot\|$ denotes Euclidean norm. Geometrically, a fluid parcel located at x_0 at time $t = t_0$ travels a length M during the period from $(t_0 - \tau)$ to $(t_0 + \tau)$. Small values of M indicate parcels that travel short distances and therefore are prone to stirring/mixing (Manney & Lawrence, 2016). Our calculation of trajectories is carried out in a cartesian coordinate system to avoid issues at the pole, and uses a Cash-Karp Runge-Kutta scheme for advancing in time. The reader is referred to Curbelo et al. (2017) and references therein for a full description of our methodology to compute trajectories. The curves on isentropic surfaces where $\|\nabla M\|$, the euclidean norm of the horizontal gradient of M , has large magnitudes approximate manifolds that act as instantaneous flow barriers (Mancho et al., 2013). In the figures that follow, $\tau = 10$ days was taken for M , and 0.7 was taken as the threshold value of $\|\nabla M\|$ normalized over the northern hemisphere for the manifolds. We determined by experimentation that these values for τ and the threshold for $\|\nabla M\|$ capture the features of M and its manifolds that we wish to highlight. The intersections of the curves corresponding to unstable and stable manifolds give the approximate locations of HTs. Parcels asymptotically approach HTs along stable manifolds and move away from them along unstable manifolds. The presence of HTs in the flow indicates regions subjected to intense deformation and mixing (García-Garrido et al., 2017; Ottino, 1989).

Of primary importance to our study is that M provides a visualization of the (kinematic) vortex boundary that is helpful in transport studies. Curbelo et al. (2019b) employed arguments of ergodic theory to conjecture that, on either a horizontal or an isentropic surface, a region where the values of M computed with sufficiently large τ has values that are very close to their maximum on the surface (M_{\max}) would, (a) materially divide the stratospheric polar vortex (SPV) core from its surroundings, and (b) be free of HTs and hence tend to not produce filaments during a certain time interval. In a nutshell, such regions represent kinematic barriers to the flow. Based on results from numerical experiments Curbelo et al. (2019b) suggested that on an isentropic surface in the stratosphere the threshold for M can be taken as the lower limit of the fat tail in its probability density function (PDF), which is $\sim 0.93 M_{\max}$. In the present study, therefore, we define the kinematic vortex boundary at an isentropic level as the region bounded by the contour where $M = 0.93M_{\max}$. Note that according to this definition, the vortex boundary on each level is a two-dimensional region in which $M > 0.93M_{\max}$, rather than the single line in the criterion based on potential vorticity and the location of its maximum gradient in latitude.

3. The Vortex Split in April 2020

We set the vortex split date on April 22 from inspection of the trajectories of parcels on the vortex boundary shown in Movie S1. Figure 1 presents the evolution of the flow in the 10-day period before the split in the form of snapshots of M and O_3 at the 530 K isentropic surface. The plot of M on April 10 captures a well-defined (cyclonic) vortex primarily symmetric about the North Pole. This is associated with an HT around ($45^\circ W, 45^\circ N$). Inspection of the Hovmöller diagrams at 50 hPa (~ 530 K) (Figure S1) shows that the latitude of this HT corresponds to the critical level for wave 1, which is traveling eastward at the time. Such a relationship between HTs and critical latitudes of planetary waves was pointed out by Guha et al. (2016). The unstable manifold extends west from this HT and imprints a clear signature on the large O_3 values over North America. Although it is not as well defined, there is another HT near the outer periphery of the vortex at around ($155^\circ W, 65^\circ N$). This HT is around the critical latitude for wave 2, which is also traveling eastward at the time. From this HT, a plume of large O_3 values extends over the northern Pacific. The O_3 plots also show how the manifolds enclose the region of very low values inside the vortex. The plot of M on April 15 shows clear changes from 5 days earlier. The vortex still flows around the pole, but its shape is more triangular as zonal wavenumber 3 has amplified (Figure S1). The HTs detected on April 10 have moved eastward and another one can be discerned around ($140^\circ E, 50^\circ N$). The imprints of the HTs on O_3 are clearly visible in the plots of these quantities. The patterns of all quantities change dramatically from April 15 to 20. M reveals that the vortex has pinched between high centers over the Pacific and Atlantic Oceans with large equatorward displacements of vortex air over North America. Another HT has developed very near the pole in association with the amplification of zonal wavenumber 2 (see Figure S1).

The configuration of the manifolds associated with the polar HT plays a key role in the vortex split. To visualize this key role, we must look at Figure 1 column (c), which corresponds to April 20, that is, just 2 days before the split. For a conceptual view of this configuration, the reader is referred to the schematics

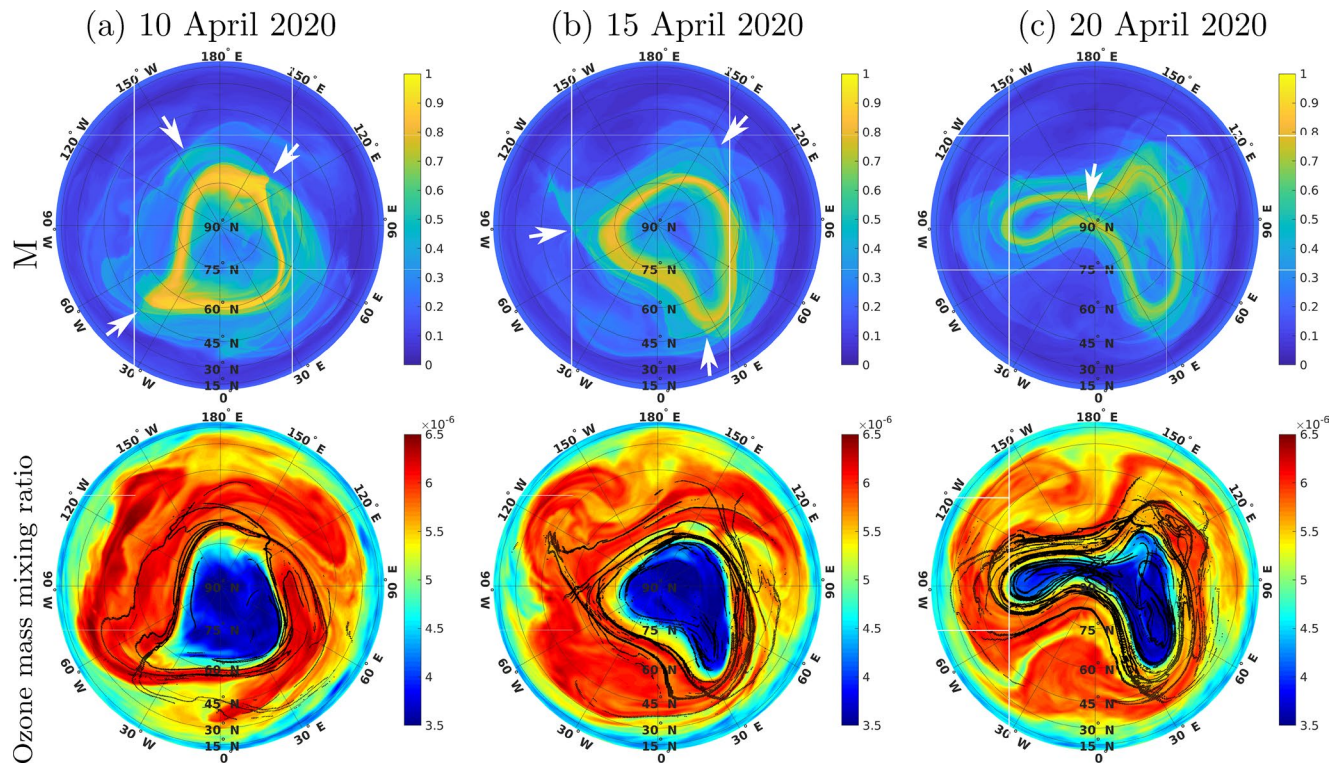


Figure 1. Maps at the 530 K isentropic surface of the normalized Lagrangian descriptor M (upper row) and ozone mass mixing ratio [kg/kg] (lower row) on (a) April 10, 2020, (b) April 15, 2020 and (c) April 20, 2020 in orthographic projection. The integration intervals for M (see the definitions in Equation 1) are March 31 00:00:00–April 20 00:00:00, April 5–25 00:00:00, and April 10–30 00:00:00, respectively. The black lines correspond to large values of $\| \nabla M \|$ and thus highlight the singular features of the function M approximating the manifolds locations. White arrows mark the hyperbolic trajectory locations referenced in the text.

in Figure S2, which is adapted for the northern hemisphere from Figure 10 in Curbelo et al. (2019a). Fluid parcels traveling at higher speeds—as evidenced by the larger values of M —from the periphery of the vortex in the eastern hemisphere to the periphery of the vortex in the western hemisphere first approach the polar HT along the stable manifold and next move away from it along the unstable manifold. As the parcels return to the eastern hemisphere, their path to the polar HT is obstructed by the manifolds that have formed ahead. For a while, some of the parcels keep circling around the vortex in the western hemisphere while others can reach the other vortex. This transfer was interrupted when the two vortices split on April 22.

The behaviors described in the previous paragraph are further illustrated by the trajectories of parcels inside the vortex boundary at 530 K in Figure 2. Using the same notation as in Movie S1, this figure shows parcel trajectories computed forward in time and colored either blue or red according to whether the initial locations are along the outside or inside edge of the boundary, that is, equatorward or poleward of the maximum value of M at each longitude at starting time. Recall that the kinematic vortex boundary is defined as the region where $M > 0.93M_{\max}$ and thus it is an area (or a strip) rather than a single line. On April 19, the colored parcels surround the considerably deformed vortex. One day later, on April 20 at 12:00:00 UTC (Figure 2c), the blue parcels in the subset labeled (A) are returning over northern North America to the vortex in the western hemisphere, in a configuration that strongly resembles the schematics in Figure S2a. The blue parcels in the subset (B) keep circling around the vortex in the eastern hemisphere while those in the subset (C) are still traveling to the other vortex. The vortex split is completed 2 days later, on April 22, for which plots are presented in the next section.

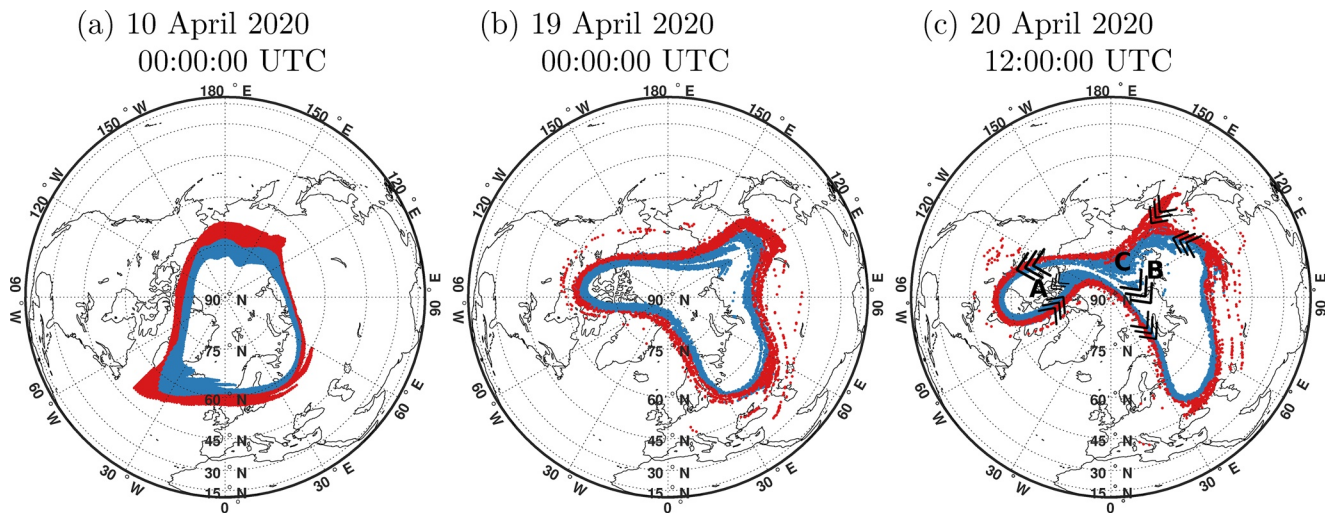


Figure 2. Panel (a) shows the locations of parcels that at 530 K on April 10, 2020 are located within contours corresponding to $M = 0.93M_{\max}$, that is, in the kinematic vortex boundary. These parcels are differentiated by blue or red colors according to whether they are along the outside or inside edge of the boundary, respectively. Panels (b) and (c) indicate the horizontal locations of the parcels in (a) at different times approaching the splitting of the main vortex on April 22 (e.g., Figure 3d). In panel (c), black arrows show the directions of motion for the parcels following the stable and unstable manifolds.

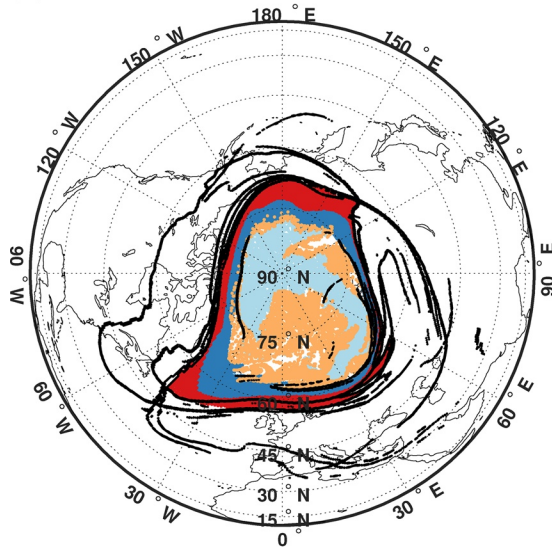
4. Transfer of Fluid Parcels Between the Vortices During and After the Split

Next, we investigate how the transfer of fluid parcels between vortices occurred at 530 K in mid-April 2020 and assess the extent to which O_3 behaved as an inert tracer. To address the transfer of fluid parcels, we plot backward trajectories starting just around the split on April 22 when O_3 values in most parcels inside both vortices are in the lower 10% for the isentropic level. The method of calculation of backward trajectories is the same as the one used to compute M . We bin those parcels with O_3 lower than 10% using either orange or light blue color according to whether O_3 is above or below 2% for the level at that time, respectively.

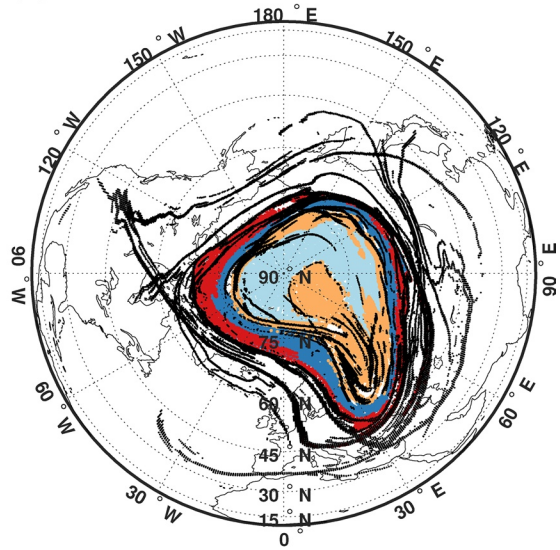
Figure 3 shows that a set of parcels with higher O_3 and encapsulated by manifolds within the main vortex core on April 10–15 moved counterclockwise along the inside edge of the vortex boundary until it was transferred to the newly formed offspring vortex over North America. To see it, panels (a)–(d) of Figure 3 shows the locations at different times of the parcels colored using the scheme described in the previous paragraph. On April 15 (panel b), the set of orange parcels with relatively high O_3 surrounded by manifolds is over Eurasia inside a U-shaped pattern formed by others in light blue with lower O_3 . Other parcels with higher O_3 remain along the vortex edge without mixing with the ozone-depleted air at the vortex core from which they are separated by manifolds. On April 10 (panel a), the configuration is broadly similar although manifolds are not clearly seen in the region covered by parcels with higher O_3 in orange color. On April 18, a large set of parcels with higher O_3 is over the North Pole. This set is also surrounded by manifolds, which indicates isolation from others inside the vortex. On April 22, one set of parcels with higher O_3 and hence labeled with orange color is inside the offspring vortex over North America while another is along the inside edge of the Eurasia vortex. Figure 3 also suggests that parcels with the lower O_3 values remained within the Eurasia vortex during the split. Movie S1 illustrates these parcel displacements with 1 h resolution.

Panels (e) and (f) of Figure 3 shows the time series of mean potential vorticity and O_3 , respectively, for the different sets of parcels represented in panels (a)–(d) of the same figure. Potential vorticity shows a slight decreasing trend. O_3 remained relatively constant, except for the set of orange parcels that show an increase around April 20. The reasons for this feature are complex and beyond the scope of this study. The vortex boundary air (red and blue parcels) has higher ozone than the interior of the vortex (orange and light blue parcels) as Figure 3f shows. Moreover, ozone values in the outer part of the vortex boundary (red line) are larger than in the inner part (blue line). This is consistent with the presence of an “ozone collar” around the vortex as reported by Mariotti et al. (2000) for the Antarctic polar vortex based on airplane data. The small range of potential vorticity and O_3 variations justifies the assumptions made about their approximate conservation during the study period. It should be noted, nonetheless, that parcels were assumed to remain

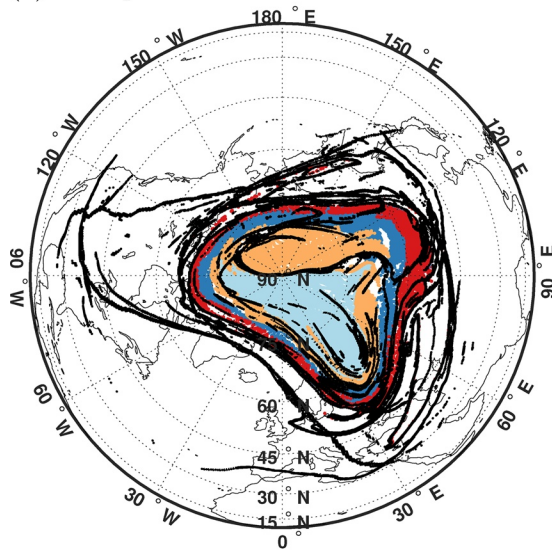
(a) 10 April 2020



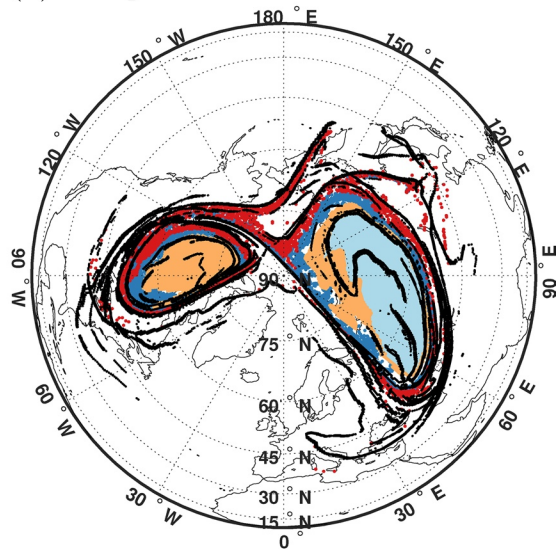
(b) 15 April 2020



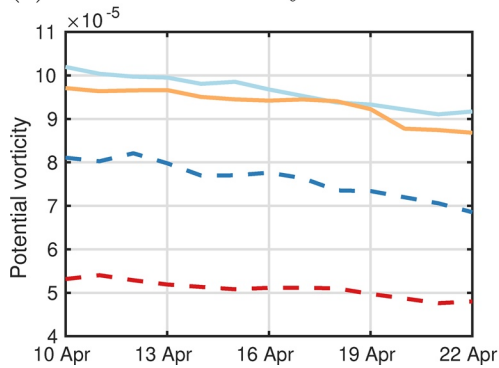
(c) 18 April 2020



(d) 22 April 2020



(e) Potential vorticity



(f) Ozone mass mixing ratio [kg/kg]

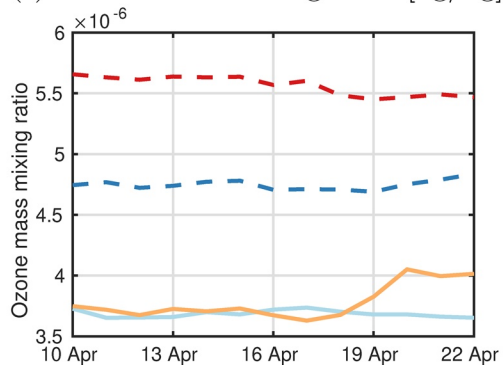


Figure 3.

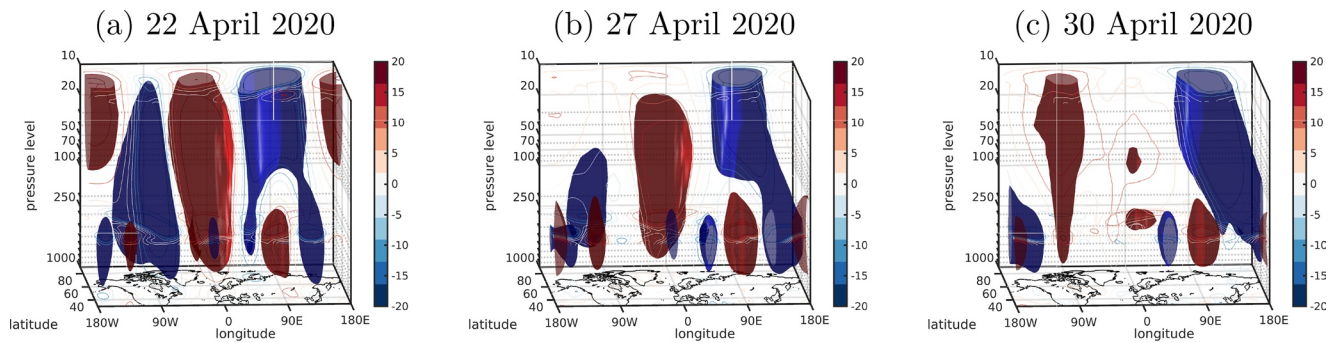


Figure 4. Three-dimensional Isosurfaces of deviations of quasi-geostrophic stream function from the zonal mean for (a) April 22, (b) April 27, and (c) April 30. Surfaces colored blue correspond to $-15 \cdot 10^6 m^2 / s$ those colored red to $15 \cdot 10^6 m^2 / s$. For added clarity, contour lines are drawn on the pressure surfaces at 1,000, 250, and 10 hPa, as well as on the vertical surface at $65^\circ N$.

on an isentropic surface and hence they did not experience any diabatic ascent or descent which may have some significance during periods of strong stratospheric disturbances (Manney et al., 1994).

To illustrate the evolution of the vortices in the stratosphere after the split we look at isosurfaces of the quasi-geostrophic (QG) stream function. Figure 4 shows deviations of this field from the zonal mean around and after the vortex split. Both vortices are very deep extending up from the troposphere, but the one over North America closes at about 20 hPa while the one over Eurasia extends above this level. In the following days, the North American vortex decays, leaving a single vortex over Eurasia by the end of April.

5. Conclusions

We have examined the period around mid-April 2020 when the main cyclonic vortex of the polar night in the northern stratosphere was displaced toward northern Eurasia from a polar position and subsequently spun off another cyclonic vortex that developed over northern North America. The two vortices remained distinct for a few days, until the final warming was completed in mid-May. Our emphasis was placed on the way in which the boundary of the main vortex ruptured to enclose two vortices, on the interactions that occurred between the vortices, and on the transfer of parcels between them that resulted in an ozone distribution where the lower values remained within the main vortex over Eurasia. The April 2020 case provided an excellent opportunity to test the hypotheses we formulated in a previous study of vortex split in the Southern Hemisphere (Curbelo et al., 2019a, 2019b), and to demonstrate how manifolds can help visualize their barrier effects on ensembles of fluid parcels. For analysis, we applied Lagrangian tools, including a Lagrangian descriptor, the estimation of HTs and associated manifolds, and a novel definition of the polar vortex boundary.

Inspection of the flow evolution before the vortex split revealed a configuration in which a polar HT plays a key role. Fluid parcels from the periphery of the vortex in the eastern hemisphere traveling at higher speeds toward near the HT along its stable manifold continued moving along the periphery of the vortex in the western hemisphere along the unstable manifold. As some of these parcels return to the eastern hemisphere, their path was obstructed by other developing manifolds and stayed circling around the vortex in the western hemisphere while others can reach the other vortex. On April 22, the transfers of fluid parcels were interrupted, and the two vortices split. Such a behavior is similar to the one described in the vortex split during the final warming of the southern stratosphere during spring 2002 (Curbelo et al., 2019b). This finding reinforces the importance of a special configuration (see also Figure S2) of a polar HT and associated

Figure 3. Panels (a)–(d) display backward parcel trajectories at 530 K that are initialized on April 22, 2020. Orange color identifies parcels that on April 22, have O_3 values between the lower 10% and 2% for the level. Light blue color identifies parcels on April 22 have O_3 values in the lower 2% for the level. Blue and red color identifies the same parcels as in Figure 2. In the maps, black lines correspond to large values of $\|VM\|$, that is, approximately the manifolds. M is calculated with $\tau = 10$ days, that is, in 20-day intervals centered on April 10 00:00:00 (a), April 15 00:00:00 (b), April 18 00:00:00 (c), April 22 00:00:00 (d). Panels (e)–(f) show the time series of mean potential vorticity and ozone mass mixing ratio for the sets of parcels.

manifolds reported by these authors. Interestingly, the features described here also mark the initiation of the intrusion of a narrow tongue of air from the tropics into the polar region between the vortices resulting from the split by Manney et al. (1994).

Around the time of the vortex split, O₃ in most parcels inside both vortices are in the lower 10% for the level. We binned these parcels according to whether O₃ was above or below 2%. Further analysis of trajectories revealed that a set of parcels with O₃ above 2% and well within the Eurasia vortex core on April 10 moved clockwise around the pole while encapsulated by manifolds until they transferred to the new offspring vortex over North America. The parcel with the lowest O₃ (below 2% for the level) remained in the main vortex in April 2020. Thus, the 2020 case gives an example of vortex split in which parcels in the offspring vortex do not necessarily come from the periphery of the main vortex. After the split, the North American vortex had a deep structure from the troposphere and disappeared after several days, leaving a single vortex over Eurasia at the end of April.

These results could provide an example for numerical models used to simulate and predict ozone loss and its impacts on climate. Analyses of model forecasts can shed light on the importance of their skills in predicting the coherent structures and manifolds we have described. Similarly, analyses of parcel trajectories binned as in the present study can indicate how well O₃ is advected during the vortex breakdown. The 2020 split is particularly notable because total column ozone values for April in the north polar region (between 50 and 90°N) derived from TROPOMI data achieved record low values (Dameris et al., 2021). Moreover, an inspection of column ozone data for April 22, 2020 shows the lowest values over Eurasia and Canada (see NASA's Ozone Watch <https://ozonewatch.gsfc.nasa.gov/NH.html>), that is, in the regions where the two vortices resulting from the split were located at the time (see Figure 3). The column ozone values in the location of these two vortices after the split were lower than in the long-term climatology. The anomalous geometrical distortions of the vortex during splits can lead to large displacements of vortex air from the polar regions to more populated regions where changes in surface UV radiation must be carefully monitored and skillfully predicted.

Data Availability Statement

The data sets used here are publicly available: ERA5, Copernicus Climate Change Service (C3S) operated by ECMWF on behalf of the European Commission. <https://doi.org/10.24381/cds.bd0915c6>. They were obtained from <https://cds.climate.copernicus.eu/cdsapp#!/dataset/10.24381/cds.bd0915c6?tab=form> (registration required).

References

- Bernhard, G. H., Fioletov, V. E., Grooß, J.-U., Ialongo, I., Johnsen, B., Lakkala, K., & Svendby, T. (2020). Record-breaking increases in arctic solar ultraviolet radiation caused by exceptionally large ozone depletion in 2020. *Geophysical Research Letters*, *47*(24), e2020GL090844. <https://doi.org/10.1029/2020gl090844>
- Bognar, K., Alwarda, R., Strong, K., Chipperfield, M. P., Dhomse, S. S., Drummond, J. R., et al. (2021). Unprecedented spring 2020 ozone depletion in the context of 20 years of measurements at Eureka, Canada. *Journal of Geophysical Research: Atmospheres*, *126*(8), e2020JD034365. <https://doi.org/10.1029/2020JD034365>
- Curbelo, J., García-Garrido, V. J., Mechoso, C. R., Mancho, A. M., Wiggins, S., & Niang, C. (2017). Insights into the three-dimensional Lagrangian geometry of the Antarctic polar vortex. *Nonlinear Processes in Geophysics*, *24*(3), 379–392. <https://doi.org/10.5194/npg-24-379-2017>
- Curbelo, J., Mechoso, C., Mancho, A. M., & Wiggins, S. (2019a). Lagrangian study of the final warming in the southern stratosphere during 2002: Part II. 3D structure. *Climate Dynamics*, *53*(3–4), 1277–1286. <https://doi.org/10.1007/s00382-019-04833-x>
- Curbelo, J., Mechoso, C., Mancho, A. M., & Wiggins, S. (2019b). Lagrangian study of the final warming in the southern stratosphere during 2002: Part I. The vortex splitting at upper levels. *Climate Dynamics*, *53*(5–6), 2779–2792. <https://doi.org/10.1007/s00382-019-04832-y>
- Dameris, M., Loyola, D. G., Nützel, M., Coldewey-Egbers, M., Lerot, C., Romahn, F., & van Roozendaal, M. (2021). Record low ozone values over the arctic in boreal spring 2020. *Atmospheric Chemistry and Physics*, *21*(2), 617–633. <https://doi.org/10.5194/acp-21-617-2021>
- García-Garrido, V. J., Curbelo, J., Mechoso, C. R., Mancho, A. M., & Wiggins, S. (2017). A simple kinematic model for the Lagrangian description of relevant nonlinear processes in the stratospheric polar vortex. *Nonlinear Processes in Geophysics*, *24*(2), 265–278. <https://doi.org/10.5194/npg-24-265-2017>
- Guha, A., Mechoso, C. R., Konor, C. S., & Heikes, R. P. (2016). Modeling Rossby wave breaking in the southern spring stratosphere. *Journal of the Atmospheric Sciences*, *73*(1), 393–406. <https://doi.org/10.1175/jas-d-15-0088.1>
- Hardiman, S. C., Dunstone, N. J., Scaife, A. A., Smith, D. M., Knight, J. R., Davies, P., & Greatbatch, R. J. (2020). Predictability of European winter 2019/20: Indian ocean dipole impacts on the NAO. *Atmospheric Science Letters*, *21*(12), e1005. <https://doi.org/10.1002/asl.1005>
- Hersbach, H., Bell, B., Berrisford, P., Biavati, G., Horányi, A., Muñoz Sabater, J., et al. (2018). ERA5 hourly data on pressure levels from 1979 to present. Copernicus Climate Change Service (C3S) Climate Data Store (CDS). <https://doi.org/10.24381/cdsbd0915c6>

Acknowledgments

The authors thank the anonymous referees for their helpful suggestions and constructive comments. Support was provided by the U.S. NSF Grant AGS-1832842. J. Curbelo also acknowledges the support of the RyC project RYC2018-025169 and 2020/2021 "L'Oréal-UNESCO For Women in Science" Fellowship (L'Oréal Spain).

- Inness, A., Chabrilat, S., Flemming, J., Huijnen, V., Langenrock, B., Nicolas, J., et al. (2020). Exceptionally low arctic stratospheric ozone in spring 2020 as seen in the CAMS reanalysis. *Journal of Geophysical Research: Atmospheres*, 125. e2020JD033563. <https://doi.org/10.1029/2020JD033563>
- Jung, J.-H., Konor, C. S., Mechoso, C. R., & Arakawa, A. (2001). A study of the stratospheric major warming and subsequent flow recovery during the winter of 1979 with an isentropic vertical coordinate model. *Journal of the Atmospheric Sciences*, 58(17), 2630–2649. [https://doi.org/10.1175/1520-0469\(2001\)058<2630:asotsm>2.0.co;2](https://doi.org/10.1175/1520-0469(2001)058<2630:asotsm>2.0.co;2)
- Lawrence, Z. D., Perlwitz, J., Butler, A. H., Manney, G. L., Newman, P. A., Lee, S. H., & Nash, E. R. (2020). The remarkably strong arctic stratospheric polar vortex of winter 2020: Links to record-breaking arctic oscillation and ozone loss. *Journal of Geophysical Research: Atmospheres*, 125(22), e2020JD033271. <https://doi.org/10.1029/2020jd033271>
- Lee, S. H., Lawrence, Z. D., Butler, A. H., & Karpechko, A. Y. (2020). Seasonal forecasts of the exceptional northern hemisphere winter of 2020. *Geophysical Research Letters*, 47(21), e2020GL090328. <https://doi.org/10.1029/2020gl090328>
- Mancho, A. M., Wiggins, S., Curbelo, J., & Mendoza, C. (2013). Lagrangian descriptors: A method for revealing phase space structures of general time dependent dynamical systems. *Communications in Nonlinear Science and Numerical Simulations*, 18(12), 3530–3557. <https://doi.org/10.1016/j.cnsns.2013.05.002>
- Manney, G. L., Farrara, J. D., & Mechoso, C. R. (1994). Simulations of the February 1979 stratospheric sudden warming: Model comparisons and three-dimensional evolution. *Monthly Weather Review*, 122(6), 1115–1140. [https://doi.org/10.1175/1520-0493\(1994\)122<1115:softss>2.0.co;2](https://doi.org/10.1175/1520-0493(1994)122<1115:softss>2.0.co;2)
- Manney, G. L., & Lawrence, Z. D. (2016). The major stratospheric final warming in 2016: Dispersal of vortex air and termination of Arctic chemical ozone loss. *Atmospheric Chemistry and Physics Discussions*, 16(23), 15371–15396. <https://doi.org/10.5194/acp-16-15371-2016>
- Manney, G. L., Lawrence, Z. D., Santee, M. L., Livesey, N. J., Lambert, A., & Pitts, M. C. (2015). Polar processing in a split vortex: Arctic ozone loss in early winter 2012/2013. *Atmospheric Chemistry and Physics*, 15(10), 5381–5403. <https://doi.org/10.5194/acp-15-5381-2015>
- Manney, G. L., Livesey, N. J., Santee, M. L., Froidevaux, L., Lambert, A., Lawrence, Z. D., et al. (2020). Record-low arctic stratospheric ozone in 2020: MLS observations of chemical processes and comparisons with previous extreme winters. *Geophysical Research Letters*, 47(16), e2020GL089063. <https://doi.org/10.1029/2020GL089063>
- Mariotti, A., Mechoso, C. R., Legras, B., & Daniel, V. (2000). The evolution of the ozone “Collar” in the Antarctic lower stratosphere during early August 1994. *Journal of the Atmospheric Sciences*, 57(3), 402–414. [https://doi.org/10.1175/1520-0469\(2000\)057<0402:teotoc>2.0.co;2](https://doi.org/10.1175/1520-0469(2000)057<0402:teotoc>2.0.co;2)
- Ottino, J. M. (1989). *The kinematics of mixing: Stretching, chaos, and transport* (Reprinted 2004). Cambridge University Press.
- Stewartson, K. (1977). The evolution of the critical layer of a Rossby wave. *Geophysical & Astrophysical Fluid Dynamics*, 9(1), 185–200. <https://doi.org/10.1080/03091927708242326>
- Warn, T., & Warn, H. (1978). The evolution of a nonlinear critical level. *Studies in Applied Mathematics*, 59(1), 37–71. <https://doi.org/10.1002/sapm197859137>
- Wohltmann, I., von der Gathen, P., Lehmann, R., Maturilli, M., Deckelmann, H., Manney, G. L., et al. (2020). Near-complete local reduction of arctic stratospheric ozone by severe chemical loss in spring 2020. *Geophysical Research Letters*, 47(20), e2020GL089547. <https://doi.org/10.1029/2020GL089547>